The following publication Jing Yao, Yufeng Gao, Yixuan Yin, Puxiang Lai, Shiwei Ye, and Wei Zheng, "Exploiting the potential of commercial objectives to extend the field of view of two-photon microscopy by adaptive optics," Opt. Lett. 47, 989-992 (2022) is available at https://dx.doi.org/10.1364/OL.450973.

# Exploiting the potential of commercial objectives to extend the field-of-view of two-photon microscopy by adaptive optics

**JING YAO,[1,2] YUFENG GAO,[1,2] YIXUAN YIN,[1,2] SHIWEI YE,[1,2,*] AND WEI ZHENG[1,2,*]**

*[1]Research Center for Biomedical Optics and Molecular Imaging, Shenzhen Key Laboratory for Molecular Imaging, Guangdong Provincial Key Laboratory of Biomedical Optical Imaging Technology, Shenzhen Institutes of Advanced Technology, Chinese Academy of Sciences, Shenzhen 518055, China*

*[2] CAS Key Laboratory of Health Informatics, Shenzhen Institutes of Advanced Technology, Chinese Academy of Sciences, Shenzhen 518055, China*

**Corresponding author: shiwei.ye@siat.ac.cn, zhengwei@siat.ac.cn*

**Two-photon microscopy (TPM) has provided critical *in situ* and *in vivo* information in biomedical studies due to its high resolution, intrinsic optical sectioning, and deep penetration. However, its relatively small field of view (FOV), which was usually determined by objectives, restricts its wide application. In this paper, we propose a segment-scanning sensorless adaptive optics method to extend the FOV and achieve high-resolution and large-FOV two-photon imaging. We demonstrated the proposed method by imaging fluorescent beads, cerebral nerve cells of mouse brain slices, and cerebral vasculature and microglia of live mice. The method extended the FOV of a commercial objective from 1.8 to 3.46 mm while maintaining a lateral resolution of 840 nm and high signal-to-noise ratio. Our technology is compatible with a standard TPM and can be used for large-scale biological exploration.**

Two-photon microscopy (TPM) enables the observation of cellular and subcellular dynamics and functions in deep nervous tissues, providing critical *in situ* and *in vivo* information for understanding neurological mechanisms [1, 2]. However, conventional TPM retains cellular resolution imaging over only a restricted field of view (FOV) of approximately 0.5 × 0.5 $mm^2$, impeding the simultaneous visualization of large area phenomena such as the multi-region neuronal activity in mammalian brain [3-6]. A previous study revealed that the objective is the key issue in determining the FOV of TPM [5, 6]. Objectives with a small numerical aperture (NA) and low magnification could provide a large observation area. Therefore, commercially available objectives with low magnification were chosen for large FOV imaging. However, the relatively small NA of these objectives restricts their application in high-resolution TPM imaging [6, 7]. Furthermore, TPM heavily relies on a tight focus to generate fluorescence signal because TPM is a nonlinear optical process. Therefore, a small NA objective is not suitable for TPM imaging. In the past decade, considerable efforts have been made to design and fabricate objectives with high NA and low magnification. Several TPM systems have been reported with custom design objectives, such as twin region panoramic 2-photon microscope (Trepan2p) [8], 2-photon random access mesoscope (2p-RAM) [9], real-time, ultra-large-scale, high-resolution (RUSH) imaging platform [10], and extremely large FOVs with high-resolution imaging have been achieved. However, these systems entail a sophisticated design and assembly of customized optical components, which significantly limits their acceptance and use by biologists. A commercial objective with a high NA that could provide a large FOV would be desirable, such that a standard TPM system could be used without significant changes.

In general, the diameter of the nominal FOV ($d_n$) of an objective is given by [5]

$$d_n = \frac{FN}{M} \tag{1}$$

where $FN$ and $M$ are the field number and magnification of the objective, respectively. The nominal FOV recommended by the objective vendor reflects the maximum imaging area where the optical aberration is considerably corrected. For an aberration-free and vignetting-less TPM, the optical invariant is conserved as a constant value in each system component and used to evaluate the throughput of the developed system. The optical invariant is given as [6]

$$I = r_m \sin\theta_m = r_o \sin\theta_o = n r_f \sin\alpha \tag{2}$$

where $r_m$ and $\theta_m$ are the beam radius and the scan angle at the scanner, and $r_o$ and $\theta_o$ are the beam radius and the incident angle of the collimated light at the objective pupil; $n$ is the refractive index of the immersion between the objective and the specimen; $r_f$ is the FOV radius, and $\alpha$ is half of the angle of the cone of light at the image plane. Typically, the nominal FOV corresponds to a small value of $\theta_o$. Occasionally, we found that the optical signals also can be detected from the area outside the nominal FOV, termed as the extended FOV (indicated as the outer annulus in Fig. 1(a)). However, the

detected image in the extended FOV is extremely blurred and dimmed because of significant aberrations (Fig. 1(a)).

In this letter, we propose a simple and effective method to extend the FOV of a commercial objective using adaptive optics (AO). Our results show that the optical aberration in the extended FOV of commercial objectives can be almost corrected by a segment-scanning sensorless AO method. Our method enables an imaging FOV diameter up to 3.46 mm wide while maintaining a lateral resolution of ~840 nm. We demonstrated the feasibility of our method by imaging fluorescent beads, nerve cells *in vitro*, and cerebral microglia vasculature of a live mouse.

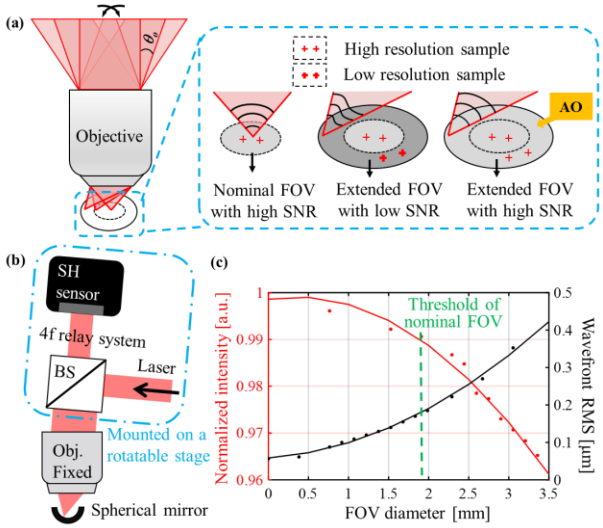


**Fig. 1.** (a) Schematic diagram of the proposed method. (b) Schematic diagram of measuring the aberrations of the objective. (c) Measured intensities and aberrations of the objective at different FOV diameters.

To clearly understand the performance of light irradiation in the extended FOV of objectives, we measured the light intensities and wavefronts at different FOV diameters. The measured objective is a commercial objective (Olympus XLPLN10XSVMP, nominal FOV= 1.8 mm). Firstly, for the intensity measurement, the collimated beam was irradiated into the objective mounted on a motorized rotation stage. We rotated the objective along its central axis and measured the corresponding intensity after the objective with a power meter (sensor: S121C, controller: PM100D, Thorlabs). The measured values were normalized by the value at the FOV center and plotted as a red line in Fig. 1(c). Although the intensity decreased as the FOV diameter increased, there was still evident light irradiation in the extended FOV (a ratio of 0.96, even at an FOV diameter of 3.5 mm). Then, we measured the wavefronts at the corresponding FOV diameters using a Shack-Hartmann wavefront sensor (provided by Nanjing Donglilai Optics & Electronics Enterprise Co., Ltd.). As shown in Fig. 1(b), a spherical mirror was carefully placed on the focal plane of the objective to reflect the beam along the original incident path. In addition, except the objective and the spherical mirror, other parts were mounted on a rotatable stage, which can rotate the incident beam along the center of the back aperture of the objective. Figure 1(c) also presents the measured wavefront root mean square (RMS) values (black line). Compared with the nominal FOV, dramatically increased aberrations can be found in the extended FOV. In summary, even almost incident light can reach the extended FOV of the objective, the large aberrations will lead to distorted point spread function and poor imaging quality.

A segment-scanning sensorless AO method was proposed to correct the large optical aberrations in the extended FOV and achieve high-resolution and high signal-to-noise ratio (SNR) imaging across a large area. The principle of the proposed AO method is as follows. (1) The entire FOV to be measured is divided into $N \times N$ subregions, and aberration correction is performed regionally. This is because the aberrations vary dramatically across the entire FOV and cannot be compensated by one wavefront pattern. Segmentation is achieved by controlling the scan mirrors. Considering both the compensation accuracy and the measurement efficiency, $3 \times 3$ subregions were used in this study. (2) For each subregion, an iterative method is used to search the optimized coefficients of the aberration modes according to the image quality metric by measuring a uniform fluorescence slice. Here, the average image intensity was chosen as the metric function. Zernike polynomials are used to represent the basic aberration modes because they form a complete orthogonal set of functions defined over a unit circle. Figure 2(a) lists the applied Zernike polynomials. For each applied Zernike polynomial, the coefficient is changed from -3 to 3 in increments of 0.5, and the corresponding wavefront pattern is successively loaded using a spatial light modulator (SLM). Subsequently, the images excited from a uniform fluorescence slice are collected to obtain the optimized coefficient that maximized the average image intensity. The determined Zernike mode must be iterated to calculate the following Zernike mode [11]. Three repeated measurements were performed to ensure the compensation accuracy. The superposition of all the calculated Zernike modes represents the overall aberration of the corresponding subregion. (3) The measured aberrations were used for other large-scale biological imaging in this letter. In practical measurement, a synchronous control of the scan engine and SLM was designed and performed to compensate for the aberrations across the entire FOV.

As shown in Fig. 2(b), a light from a Ti: Sapphire laser (Chameleon Ultra II, Coherent) was expanded to utilize the maximal effective area of the SLM (PLUTO-BB II, Holoeye Photonics). A half-wave plate was placed before the SLM to orientate the polarization of the laser to match the SLM. Then, the light successively passed through Galvos XY (TSH8618, SUNNY) and the objective (XLPLN10XSVMP, Olympus) to form a tight spot in the specimen. To ensure accurate projection of the phase pattern, the SLM, the paired galvanometers, and the objective rear pupil plane were mutually conjugated by three relay engines (RE1, RE2: two off-axis parabolic mirrors, f=50.8 mm; RE3: a scan lens (LSM54-850, Thorlabs) and a tube lens (88596, RFL=200 mm, Edmund)). The fluorescence collected from the sample was reflected by a dichroic mirror (T725lpxrxt-UF3, Chroma) and collected by a photomultiplier tube (CH345, Hamamatsu). A National Instruments DAQ card (PCI-6110) was used to control and synchronize the system as well as digitize the signal. Experimentally, we tuned the correction collar of the employed objective to minimize the system-induced spherical aberration. Then, the proposed segment-scanning sensorless AO method was used to measure the remaining aberrations of 3×3 subregions across the entire FOV (Fig. 2(c)). It is found that the measured wavefronts were almost rotationally symmetric. In the extended FOV, the astigmatism and the coma are the main sources of the large off-axis aberrations. In order to know whether these aberrations indeed come from the objective, we also measured the

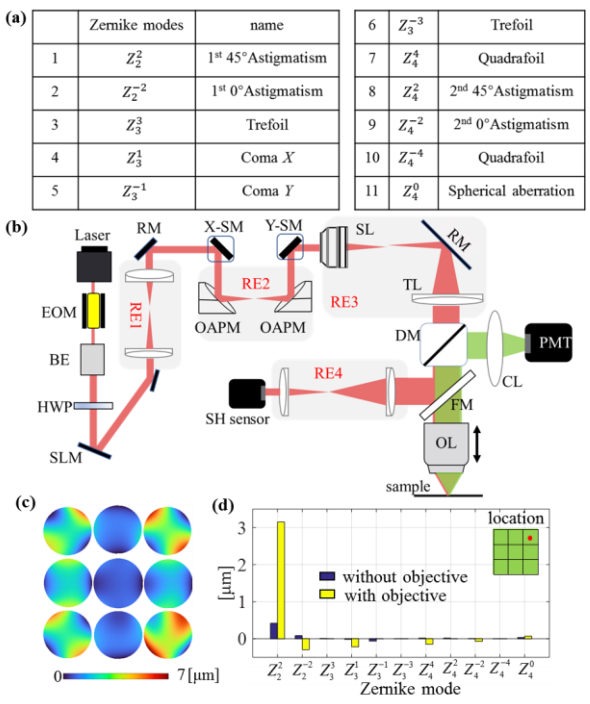


| | Zernike modes | name | | | |
|---|---|---|---|---|---|
| 1 | $Z_2^2$ | 1st 45°Astigmatism | 6 | $Z_3^{-3}$ | Trefoil |
| 2 | $Z_2^{-2}$ | 1st 0°Astigmatism | 7 | $Z_4^4$ | Quadrafoil |
| 3 | $Z_3^3$ | Trefoil | 8 | $Z_4^2$ | 2nd 45°Astigmatism |
| 4 | $Z_3^1$ | Coma $X$ | 9 | $Z_4^{-2}$ | 2nd 0°Astigmatism |
| 5 | $Z_3^{-1}$ | Coma $Y$ | 10 | $Z_4^{-4}$ | Quadrafoil |
| | | | 11 | $Z_4^0$ | Spherical aberration |

**Fig. 2.** (a) The applied Zernike polynomials. (b) Schematic diagram of the developed TPM system. EOM, Electro-optic modulator; RM, Reflective mirror; BE, Beam expander; SLM, Spatial Light Modulator; OAP, Off-axis parabolic mirror; SM, Scan Mirror; SL, Scan lens; TL, Tube lens; DM, Dichroic Mirror; OL, Objective Lens; CL, Collective Lens; FM: Flip mirror. (c) Measured wavefronts of 3×3 subregions. (d) Comparison of the measured wavefronts with and without the objective in one subregion of the extended FOV.

aberrations without the objective. A flip mirror was used to reflect the beam into a Shack-Hartmann sensor conjugated with the objective rear pupil plane (Fig. 2(b)). The results in a same region of the extended FOV with and without objective were compared in Fig. 2(d). The aberration caused by other components of the developed system is negligible compared to the objective-induced aberration.

The feasibility of the proposed method was first verified by measuring 1-μm fluorescent beads. We prepared a gel with fluorescent beads by mixing 5 μL fluorescent beads (F8852, Thermo Fisher) with 1 mL of 1% agarose solution. Figure 3(a) shows the captured image of fluorescence beads within an FOV diameter of 3.46 mm by the proposed method. Two regions of interest (ROI) in the nominal and extended FOV are magnified in Figs. 3(b) and (c), respectively. The proposed AO correction had almost no effect on the nominal FOV, whereas some blurred and dimmed beads in the extended FOV became distinguishable after AO correction. The normalized intensity profiles of a single fluorescence bead from the nominal and extended FOV are illustrated in Figs. 3(d)–(g). The results suggest that the proposed AO method can effectively improve the peak intensity of the measured fluorescent beads by a factor of five in the extended FOV. Moreover, we measured the spatial resolution across the entire FOV using 500-nm fluorescent beads (F8813, Thermo Fisher). After AO correction, the measured lateral and axial resolutions were ~700 ± 20 nm and ~5.1 ± 0.4 μm (theoretical lateral and axial resolutions are 550 nm and 4.03 μm) in the nominal FOV, and ~840 ± 40 nm and ~5.8 ± 0.4 μm in the extended FOV, respectively. This indicates that the proposed method can effectively extend the imaging FOV of a commercial objective and achieve large-area two-photon imaging

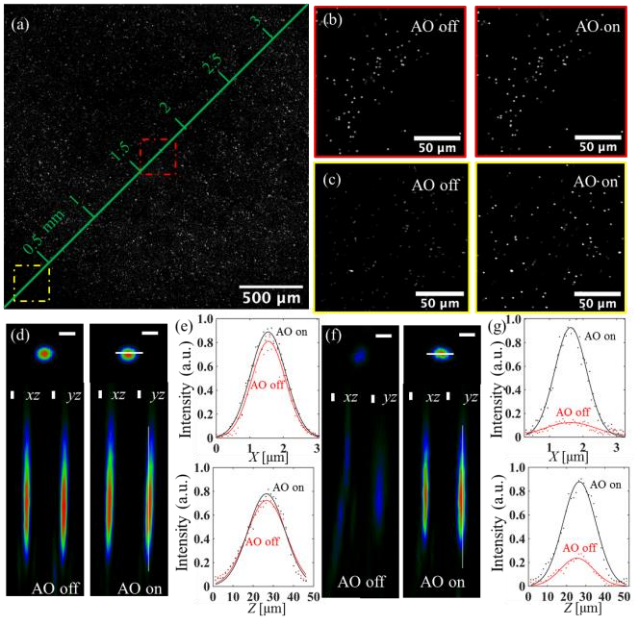


**Fig. 3.** Imaging of 1-μm fluorescent beads within a FOV diameter of 3.46 mm. (a) The lateral view within the entire imaging FOV by the proposed method. (b, c) Comparison of ROIs (indicated as red and yellow boxes in (a)) in the nominal and extended FOV with and without AO correction. Three views and normalized intensity profiles of single fluorescence bead: (d, e) in the nominal FOV; (f, g) in the extended FOV.

while maintaining a sub-micrometer lateral resolution and high SNR. The difference between the theoretical and measured resolutions might be explained by the correction inaccuracy due to the size of subregion and the sample-induced aberration. We also compared the system-induced aberration and sample-induced aberration in the same region of the extended FOV. The measured wavefront RMS of sample-induced aberration was less than 5% of that of system-induced aberration. Further, considering that the proposed method is still time-consuming, we omitted the compensation of sample-induced aberrations in this letter.

For *in vitro* imaging, a 200-μm-thick slice from Thy1-GFP-M mice (Stock No. 007788, Jackson Laboratory) was used as the imaging sample. Figure 4(a) shows the lateral view (max intensity project, MIP) of the measured cerebral nerve cells in an FOV of 2.45 × 2.45 mm$^2$ by the proposed method, which revealed almost 1/4 of the entire mouse brain area. To verify the effect of the proposed AO correction, we magnified one ROI in the extended FOV and presented the results with and without AO correction in Fig. 4(b). Furthermore, three-dimensional (3D) views of smaller ROIs are shown in Fig. 4(c). Compared with the results without AO correction, some somas and axons can be more clearly observed after AO correction. Figure 4(d) shows a frame extracted from another ROI at a depth of 16 μm, and the intensity profile of the line-outs marked in Fig. 4(d) is illustrated in Fig. 4(e). Evidently, the proposed method sharpened the image and resulted in an axon with a finer width. Furthermore, the peak intensity was improved by a factor of ~5, which is consistent with the results obtained by measuring fluorescent beads.

Finally, we provide some results of *in vivo* imaging of mouse cerebral microglia and vasculature. For *in vivo* imaging, we made a 5-mm-diameter cranial window on CX3CR1-GFP mice to observe the cerebral microglia, and on BALB/c mice injected with FITC dye to observe the cerebral vasculature. Figure 5(a) shows the lateral

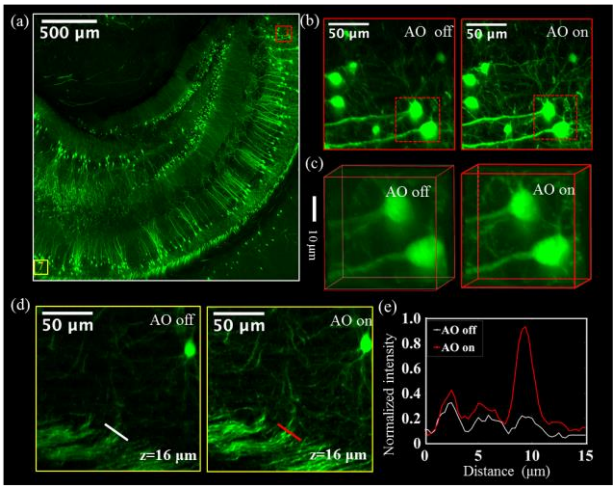


**Fig. 4.** Large FOV imaging of the Thy1-GFP-M mice brain slice. (a) Lateral view (MIP) with an entire FOV of 2.45 × 2.45 mm$^2$ by the proposed method. (b) Comparison of one ROI (indicated as red box in (a)) in the extended FOV between AO on and AO off. (c) Further comparison (indicated as red box in (b)) of 3D views. (d) Comparison of one frame extracted from another ROI (indicated as yellow box in (a)) between AO on and AO off. (e) Normalized intensity of the line-outs marked as white and red lines in (d).

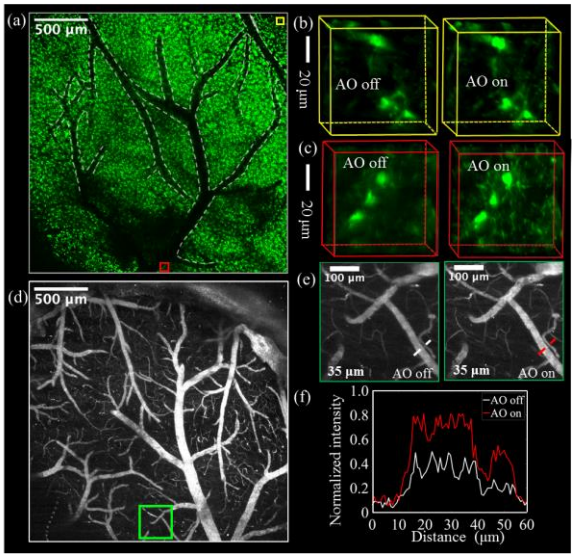


**Fig. 5.** *In vivo* imaging of the mouse cerebral microglia and vasculature with a large FOV. (a) Lateral view (MIP) of mice cerebral microglia with an entire FOV of 2.45 × 2.45 mm$^2$ by the proposed method. (b, c) Comparison of two ROIs (indicated as red and yellow boxes in (a)) in the extended FOV between AO on and AO off. (d) Lateral view (MIP) of mice cerebral microglia with an entire FOV of 2.45 × 2.45 mm$^2$. (e) Comparison of one frame extracted from the ROI (indicated as green box in (d)) between AO on and AO off. (f) Normalized intensity of line-outs marked as white and red lines in (e).

view (MIP) of the cerebral microglia with a FOV of 2.45× 2.45 mm$^2$ by the proposed AO correction. The 3D views of two ROIs in the extended FOV with and without AO correction are compared in Figs. 5(b) and (c), respectively. Evidently, both the cell body and the process of microglia became more distinguishable after AO correction. Figure 5(d) presents the mouse cerebral vasculature (MIP) with the same FOV as in Fig. 5(a) by the proposed method. The cerebral vasculature distribution in live mice can be clearly observed across a large area. Furthermore, we extracted a frame from one ROI and compared the results of the cerebral vasculature with and without AO correction (Fig. 5(e)). The intensity profiles of the line-outs marked in Fig. 5(e) are plotted in Fig. 5(f). The peak intensity of blood vessels was enhanced, and some fine vessels became more distinct after AO correction. The results indicate that the proposed method can effectively exploit the potential of commercial objectives to achieve high-resolution, high SNR, and large-FOV two-photon imaging for *in vivo* observation.

In summary, we proposed and implemented a segment-scanning sensorless adaptive optics method to extend the FOV of commercial objectives. The proposed method enabled high-resolution and high-SNR two-photon imaging across an FOV diameter of 3.46 mm by using a commercial objective with a nominal FOV diameter of 1.8 mm. Moreover, this technology is compatible with a standard TPM and requires no sophisticated design or assembly of customized optical components. Our method will motivate large-scale exploration of brain networks and neural phenomena. For the applied objective, $\theta_0$ is limited to 5-6° to circumvent the vignetting. However, the achievable FOV diameter of developed TPM was also limited by the throughput of the scan lens. If a higher angle (larger than 3.5°) is applied, the incident angle will exceed the maximal scan angle and the beam will be clipped by the scan lens. In future work, we intend to increase the 3D imaging speed across a large imaging FOV and further study cerebral neural circuits.

**Funding.** Support for this work was provided by the National Key Research and Development Program of China (2017YFC0110200), National Natural Science Foundation of China (81822023, 81927803, 91959121, 62105353), Natural Science Foundation of Guangdong Province (2020B121201010, 2021A1515012022), the Scientific Instrument Innovation Team of the Chinese Academy of Sciences (GJJSTD20180002), and the Shenzhen Basic Research Program (JCYJ20170818164343304, JCYJ20180507182432303, ZDSY20130401165820357), SIAT Innovation Program for Excellent Young Researchers (E1G029).

**Disclosures.** The authors declare no conflicts of interest.

**Data availability.** Data underlying the results presented in this paper are not publicly available at this time but may be obtained from the authors upon request.

## References

1. J. H. Marshel, M. E. Garrett, I. Nauhaus, and E. M. Callaway, Neuron **72**(6), 1040–1054 (2011).
2. R. Lu, W. Sun, Y. Liang, A. Kerlin, J. Bierfeld, J. D. Seelig, D. E. Wilson, B. Scholl, B. Mohar, M. Tanimoto, M. Koyama, D. Fitzpatrick, M. B. Orger, and N. Ji, Nat. Neurosci. **20**(4), 620–628 (2017).
3. W. Yang and R. Yuste, Nat. Methods **14**(4), 349–359 (2017).
4. Y. Masamizu, Y. Tanaka, Y. Tanaka, R. Hira, F. Ohkubo, K. Kitamura, Y. Isomura, T. Okada, M. Matsuzaki, Nat. Neurosci. **17**(7), 987–994 (2014).
5. N. Ji, J. Freeman, and S. L. Smith, Nat. Neurosci. **19**(9), 1154–1164 (2016).
6. J. R. Bumstead, J. J. Park, I. A. Rosen, A. W. Kraft, P. W. Wright, M. D. Reisman, D. C. Cote, and J. P. Culver, Neurophotonics **5**(2), 025001 (2018).
7. P. S. Tsai, C. Mateo, J. J. Field, C. B. Schaffer, M. E. Anderson, and D. Kleinfeld, Opt. Express **23**(11), 13833–13847 (2015).
8. J. N. Stirman, I. T. Smith, M. W. Kudenov, and S. L. Smith, Nat. Biotechnol. **34**(8), 857–862 (2016).
9. N. J. Sofroniew, D. Flickinger, J. King, and K. Svoboda, Elife **5**, e14472 (2016).
10. J. Fan, J. Suo, J. Wu, H. Xie, Y. Shen, F. Chen, G. Wang, L. Cao, G. Jin, Q. He, T. Li, G. Luan, L. Kong, Z. Zheng, and Q. Dai, Nat. Photonics **13**(11), 809–816 (2019).
11. A. Facomprez, E. Beaurepaire, and D. Débarre, Opt Express **20**(3), 2598–2612 (2012)

## References


1. J. H. Marshel, M. E. Garrett, I. Nauhaus, and E. M. Callaway, "Functional specialization of seven mouse visual cortical areas," Neuron **72**(6), 1040–1054 (2011).
2. R. Lu, W. Sun, Y. Liang, A. Kerlin, J. Bierfeld, J. D. Seelig, D. E. Wilson, B. Scholl, B. Mohar, M. Tanimoto, M. Koyama, D. Fitzpatrick, M. B. Orger, and N. Ji, "Video-rate volumetric functional imaging of the brain at synaptic resolution," Nat. Neurosci. **20**(4), 620–628 (2017).
3. W. Yang and R. Yuste, "In vivo imaging of neural activity," Nat. Methods **14**(4), 349–359 (2017).
4. Y. Masamizu, Y. Tanaka, Y. Tanaka, R. Hira, F. Ohkubo, K. Kitamura, Y. Isomura, T. Okada, M. Matsuzaki, "Two distinct layer-specific dynamics of cortical ensembles during learning of a motor task," Nat. Neurosci. **17**(7), 987–994 (2014).
5. N. Ji, J. Freeman, and S. L. Smith, "Technologies for imaging neural activity in large volumes," Nat. Neurosci. **19**(9), 1154–1164 (2016).
6. J. R. Bumstead, J. J. Park, I. A. Rosen, A. W. Kraft, P. W. Wright, M. D. Reisman, D. C. Cote, and J. P. Culver, "Designing a large field-of-view two-photon microscope using optical invariant analysis," Neurophotonics **5**(2), 025001 (2018).
7. P. S. Tsai, C. Mateo, J. J. Field, C. B. Schaffer, M. E. Anderson, and D. Kleinfeld, "Ultra-large field-of-view two-photon microscopy," Opt. Express **23**(11), 13833–13847 (2015).
8. J. N. Stirman, I. T. Smith, M. W. Kudenov, and S. L. Smith, "Wide field-of-view, multi-region, two-photon imaging of neuronal activity in the mammalian brain," Nat. Biotechnol. **34**(8), 857–862 (2016).
9. N. J. Sofroniew, D. Flickinger, J. King, and K. Svoboda, "A large field of view two-photon mesoscope with subcellular resolution for in vivo imaging," Elife **5**, e14472 (2016).
10. J. Fan, J. Suo, J. Wu, H. Xie, Y. Shen, F. Chen, G. Wang, L. Cao, G. Jin, Q. He, T. Li, G. Luan, L. Kong, Z. Zheng, and Q. Dai, "Video-rate imaging of biological dynamics at centimetre scale and micrometre resolution," Nat. Photonics **13**(11), 809–816 (2019).
11. A. Facomprez, E. Beaurepaire, and D. Débarre, "Accuracy of correction in modal sensorless adaptive optics," Opt Express **20**(3), 2598–2612 (2012).